Environmental Science & Technology

Article

Cite This: Environ. Sci. Technol. 2019, 53, 10855−10862

pubs.acs.org/est

Nanodispersed Mn_3O_4/γ-Al_2O_3 for NO_2 Elimination at Room Temperature

Lian Wang,[†,§] Guangyan Xu,[†] Jinzhu Ma,[†,‡,§] Yunbo Yu,[†,‡,§] Qingxin Ma,[†,‡,§] Kuo Liu,[†] Changbin Zhang,*[,†,§] and Hong He[†,‡,§]

[†]State Key Joint Laboratory of Environmental Simulation and Pollution Control, Research Center for Eco-Environmental Sciences, Chinese Academy of Sciences, Beijing 100085, China

[‡]Center for Excellence in Urban Atmospheric Environment, Institute of Urban Environment, Chinese Academy of Sciences, Xiamen 361021, China

[§]University of Chinese Academy of Sciences, Beijing 100049, China

Supporting Information

ABSTRACT: Adsorption is an efficient method for atmospheric NO_x abatement under ambient conditions; however, traditional adsorbents suffer from limited adsorption capacity and byproduct formation. Developing a low-cost material with high capacity for atmospheric NO_2 elimination remains a challenge. Here, we synthesized a nanodispersed Mn_3O_4/γ-Al_2O_3 (Mn/Al) material that exhibits excellent ability to remove NO_2. The 10 wt % Mn/Al sample showed the highest removal capacity, with 247.6 $mg_{NO_2}/g_{Mn/Al}$, which is superior to that of activated carbon (42.6 mg_{NO_2}/g). There were no byproducts produced when Mn/Al was tested with ppb-level NO_2. The NO_2 abatement mechanism with Mn/Al is different from physisorption or chemisorption. NO_2 removal is mainly a catalytic process in air, during which surface hydroxyls and lattice oxygen are involved in the oxidation of NO_2 to nitrate. In contrast, a chemical reaction between Mn^{3+} and NO_2 is dominant in N_2, where Mn^{3+} is converted into Mn^{4+} and NO_2 is reduced to nitrite. Washing with deionized water is an effective and convenient method for the regeneration of saturated Mn/Al, and an 86% adsorption capacity was recovered after one washing. The results suggest that this low-cost Mn/Al material with easy preparation and regeneration is a promising candidate material for atmospheric NO_2 elimination.

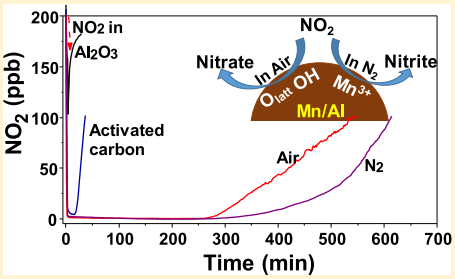

1. INTRODUCTION

Nitrogen oxides (NO_x), mainly emitted from stationary sources and vehicle engines, are considered to be some of the major atmospheric pollutants, contributing to serious environmental problems such as acid rain, photochemical smog, haze pollution, etc.[1,2] In particular, NO_x was found to greatly promote the conversion of SO_2 to sulfate,[2] reducing the environmental capacity for SO_2 and accelerating haze formation.[3−5] Thus, the abatement of NO_x is urgently needed to meet emission regulations and improve environmental quality. NO is a main component released into the atmosphere from the combustion process, and it can be easily converted to the more hazardous and oxidizing NO_2 through a photochemical oxidation reaction, nonthermal plasma catalysis (NTP) process, etc.[6−9] Therefore, the effective removal of NO_2 is of great importance and has attracted significant attention.[10−14]

To date, different technologies have been employed for NO_2 removal, including adsorption using activated carbon and zeolite, catalytic processes such as selective catalytic reduction, and photocatalysis.[10−14] Adsorption technology has been a popular subject of many studies due to its ease of use. A variety of adsorbents have been developed and evaluated for NO_2 removal, including carbon-based materials, zeolites, metal−organic frameworks (MOFs), etc.[11,15−18] Some carbon materials have demonstrated high efficiency for NO_2 removal, while some byproducts, such as NO, CO, and CO_2, are still inevitably formed during the process. MOF materials such as UiO-66-NH_2 have exhibited much higher NO_2 adsorption capacity, with reduced NO generation compared to that of commercial activated carbon.[18] However, the preparation process for MOFs is complicated and the cost is high. In addition, the framework of MOF materials is usually destroyed after use for NO_2 removal; therefore, their wide application is limited. Furthermore, in previous studies, adsorption materials such as activated carbon and zeolite have generally been tested under high NO_2 concentration (hundreds of ppm level) conditions, aiming at end-of-pipe NO_x treatment. There is less literature related to the removal of low concentrations of NO_2 (hundreds of ppb level) using adsorption materials. Moreover, adsorption materials usually have poor regeneration performance and need to be replaced once saturated. Ambient treatment of NO_2 in indoor and outdoor air is also important

Received: March 4, 2019
Revised: August 11, 2019
Accepted: August 16, 2019
Published: August 16, 2019

DOI: 10.1021/acs.est.9b00941
Environ. Sci. Technol. 2019, 53, 10855−10862

to improve air quality. In recent years, photocatalytic technology has been widely used through painting of catalysts onto indoor or outdoor buildings such as on walls and pavements.[19−25] For NO_2 abatement in indoor or outdoor air at room temperature, consequently, it is still of great significance to develop new low-cost materials with high removal efficiency.

Low-cost manganese oxides are well known as some of the most active catalysts for low-temperature SCR of NO_x.[26,27] Previous studies also demonstrated that manganese oxide-based materials are active for NO oxidation at room temperature. As suggested by Zhang et al., catalytic oxidation of NO into NO_2 can be achieved over MnO_2/carbon nanotubes at room temperature.[28] Furthermore, Zhu et al. have reported that MnO_x/Al_2O_3 could promote benzene, toluene, xylene (BTX) total conversion and reduce the emission of NO_2 in the process of nonthermal plasma catalysis.[29] In the NTP-catalysis process of *o*-xylene oxidation, our previous study also showed that a Mn/Al material could efficiently remove NO_2 produced by NTP treatment.[9] It has been suggested that NO_2 can be oxidized into NO_3^- by oxidative radicals produced by the plasma and then reduced to N_2 by the partially oxidized hydrocarbon.[30,31] Such conversion of NO_2 to NO_3^- was also observed over TiO_2 or $CuMn/TiO_2$ catalysts with NTP, thus contributing to NO_2 abatement.[32] Without involving NTP, however, there have been no studies related to NO_2 removal on Mn-based materials at room temperature.

In this study, we prepared a series of nanodispersed Mn_3O_4/γ-Al_2O_3 (Mn/Al) materials with different Mn loadings by a simple conventional impregnation method and tested their removal capacities toward NO_2. The effects of gas hourly space velocity (GHSV), NO_2 concentration, water vapor, and reaction atmosphere were investigated in detail, and the species formed on the surface of the samples were also identified. We observed that the Mn/Al materials are highly efficient for NO_2 abatement with the advantages of no byproduct formation and high tolerance to GHSV. The Mn/Al samples were next carefully characterized by X-ray diffraction (XRD), X-ray photoelectron spectroscopy (XPS), field-emission transmission electron microscopy (FESEM) mapping tests, and X-ray adsorption near-edge structure (XANES) measurements. Based on the characterization results, the role of Mn species in NO_2 adsorption and the correlating abatement mechanism were discussed and elucidated.

2. EXPERIMENTAL SECTION

2.1. Sample Preparation. Mn/Al samples with 4, 6, 8, 10, 12, and 20 wt % Mn loadings were prepared by an impregnation method by introducing an appropriate amount of γ-Al_2O_3 powder into manganese acetate solutions. In other words, the weight ratios of Mn to γ-Al_2O_3 were 4, 6, 8, 10, 12, and 20, respectively. Synthesis details can be found in the Supporting Information. For comparison, 10 wt % Mn_3O_4/Al_2O_3 and 10 wt % Mn_2O_3/Al_2O_3 samples were also prepared by mixing commercial Mn_3O_4 and Mn_2O_3 powders (Sinopharm Chemical Reagent Co., Ltd., China), respectively, with γ-Al_2O_3 powder by the ball-milling method. Commercial activated carbon (AC) powder with a surface area of 691.0 m^2/g, a pore diameter of 3.1 nm, and a pore volume of 0.61 cm^3/g (Ningxia Taixi Carbon Corporation, China) was used as a reference. AC was pretreated at 600 °C for 3 h in a helium atmosphere before being tested.

2.2. Sample Characterization. The XRD patterns of samples were obtained using an X-ray diffractometer (Bruker D8, Germany) with a Cu Kα source (λ = 0.15406 nm) operated at 40 kV and 40 mA. The surface areas of the samples were calculated by the Brunauer−Emmett−Teller (BET) method based on nitrogen adsorption−desorption isotherms obtained on a Quantachrome Autosorb-1C instrument at 77 K. Field-emission transmission electron microscope (FETEM) measurements were performed on a JEOL JEM 2010F (Hitachi, Japan) system. XPS measurements were carried out on a Thermo ESCALAB 250 spectrometer (Vacuum Generators, USA) using Al Kα radiation. The spectra were corrected by referencing the C 1s peak at 284.8 eV. The XANES of the Mn K-edge in Mn/Al samples and Mn-containing reference samples were measured on the BL14W1 beamline at the Shanghai Synchrotron Radiation Facility. In situ DRIFTS experiments were carried out on a Nicolet Nexus 670 Fourier transform infrared (FT-IR) spectrometer. The products formed on the samples were quantitatively analyzed by means of ion chromatography (IC). The experimental details can be found in the Supporting Information.

2.3. NO_2 Removal Test. The NO_2 removal tests were carried out in a continuous flow fixed-bed quartz microreactor with samples (40−60 mesh) at 25 °C. The samples were immobilized in the reactor by quartz wool. The typical reactant feed (1 L/min) was composed of either 200 ppb or 500 ppm NO_2, 20% O_2, 80% relative humidity (when used), and N_2 balance. The concentrations of 200 ppb and 500 ppm represent the ambient atmosphere and end-of-pipe emission concentrations of NO_2, respectively. The outlet gases were monitored online by a NO_x analyzer (Thermo Fisher 42i) for 200 ppb NO_2, and those for 500 ppm NO_2 by an online FT-IR (Thermo Scientific Nicolet iS50) equipped with a 2 m gas cell and a deuterated triglycine sulfate detector with a resolution of 0.5 cm^{-1} and an optical path difference velocity of 0.4747 cm s^{-1}. The experimental details can be found in the Supporting Information. NO_2 removal tests were repeated three times, and the total removal amount of NO_2 was calculated based on breakthrough curves. The removal capacities of samples were obtained by normalizing the total removal amount of NO_2 by the mass of sample, and the average values and standard deviations were also extracted. NO was also detected in the NO_2 removal process, and NO release was calculated by the ratio of the relative amount of NO produced to the total removal amount of NO_2.

3. RESULTS AND DISCUSSION

3.1. NO_2 Abatement Efficiency of Mn/Al at Room Temperature. The Mn/Al materials with 4, 6, 8, 10, 12, and 20 wt % Mn loadings were tested for 200 ppb NO_2 removal at room temperature with a high GHSV of 300 000 h^{-1}, and the NO_2 breakthrough curves of the materials studied are presented in Figure 1. All Mn/Al samples showed much higher removal capacity values than that of the commercial AC. With increasing Mn loading from 4 to 10 wt %, the removal ability gradually increased, while further increasing Mn loading resulted in a decrease in the removal efficiency. Thus, 10 wt % Mn/Al exhibited the highest removal efficiency. The pure Al_2O_3 support showed almost no removal efficiency, indicating that the Mn species played a key role in NO_2 removal. For comparison, 10 wt % Mn_3O_4/Al_2O_3 and $Mn_2O_3/$

DOI: 10.1021/acs.est.9b00941
Environ. Sci. Technol. 2019, 53, 10855−10862

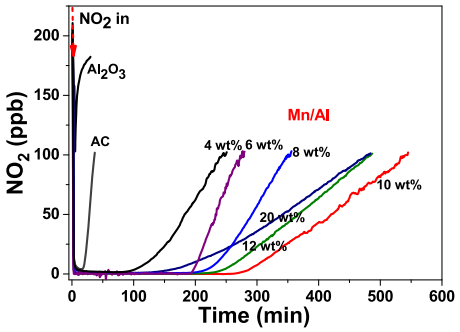

Figure 1. NO_2 breakthrough curves in air at 25 °C. Reaction conditions: NO_2, 200 ppb; Mn/Al or Al_2O_3, 0.05 g; AC, 0.025 g; total flow rate, 1 L/min (20 vol % O_2, N_2 balance); GHSV, 300 000 h^{-1}.

Al_2O_3 prepared from commercial crystalline Mn_3O_4 and Mn_2O_3 were also tested (Figure S1). The Mn_3O_4/Al_2O_3 and Mn_2O_3/Al_2O_3 mixtures exhibited a much lower removal efficiency than the Mn/Al samples, suggesting that neither highly crystalline Mn_3O_4 nor Mn_2O_3 was effective for NO_2 removal.

Previous studies showed that the initial concentration of NO_2 has a great influence on its removal efficiency,[14] and the GHSV is also an important factor influencing the reaction activity. Therefore, the removal efficiency of 10 wt % Mn/Al toward 500 ppm NO_2 was next examined at room temperature under different GHSVs and compared to that of conventional AC (Figure S2). Based on the NO_2 breakthrough curves in both Figures 1 and S2, the NO_2 removal capacities of Mn/Al and AC were calculated and are listed in Table 1. In the case of 200 ppb NO_2 under 300 000 h^{-1} GHSV, the adsorption capacity of AC was only 0.9 $mg_{NO_2}/g_{Mn/Al}$, and the 10 wt % Mn/Al possessed a removal capacity of 5 $mg_{NO_2}/g_{Mn/Al}$. This was 5 times higher than that of AC, indicating that 10 wt % Mn/Al is a highly efficient material for NO_2 removal at ppb levels at room temperature. In the case of 500 ppm NO_2 under 50 000 h^{-1} GHSV, the adsorption capacity of AC increased up to 91.1 mg_{NO_2}/g, which is consistent with values in the literature.[14,17] The removal capacity of 10 wt % Mn/Al was 175.8 mg NO_2/g, which was still two times higher than that of AC under the same conditions. The increased opportunity for contact between NO_2 and the materials should account for the improved removal capacities with the increase in initial NO_2 concentration. Changes in GHSV showed totally different effects on AC and Mn/Al for NO_2 adsorption. The increase in GHSV from 50 000 to 300 000 h^{-1} clearly decreased the adsorption capacities of AC from 91.1 to 42.6 mg NO_2/g, while it dramatically improved the removal capacities of Mn/Al from 175.8 to 247.6 NO_2/g. The different effects of GHSV are possibly due to the different NO_2 abatement mechanisms for AC and Mn/Al.

During the NO_2 abatement processes, the NO and N_2O byproducts produced were also measured (Table 1). In the case of 500 ppm NO_2, NO formation was observed on both AC and Mn/Al, while the relative amount of NO produced to total adsorbed NO_2 was lower on Mn/Al than that on AC. In the case of 200 ppb NO_2, a large amount of NO was still produced on AC. In contrast, neither NO nor N_2O was detected when Mn/Al was used. The above findings suggest that Mn/Al materials are very suitable for the elimination of low concentrations of NO_2 in the atmosphere, with the advantages of no byproduct formation and a high tolerance to GHSV.

3.2. Intrinsic Influence Factor of Different Mn Loading Amounts. The physical and structural properties of Mn/Al materials were next investigated to reveal the main reason for their high NO_2 removal efficiencies, especially for the 10 wt % Mn/Al sample. As shown in Figure 2, all samples

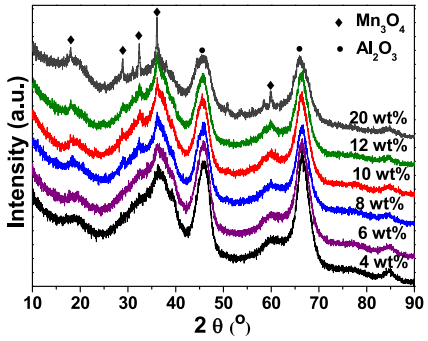

Figure 2. XRD patterns of Mn/Al samples.

exhibited the main diffraction peaks of γ-Al_2O_3 [PDF#50-0741] at 37.5, 45.7, and 66.6°. In the case of 4 and 6 wt % Mn/Al, no clear Mn-related crystalline peaks appeared. When Mn loading was increased to 20 wt %, sharp peaks due to the Mn_3O_4 phase at 18.1, 28.9, 32.4, 36.2, and 59.9° [PDF#24-0734] were observed, indicating the formation of well-crystallized Mn_3O_4, whereas XRD patterns of 8, 10, and 12 wt % Mn/Al samples presented similar but weak peaks of crystallized Mn_3O_4, implying that Mn oxides existed in a microcrystalline state.

The XANES spectra of the Mn K edge were measured to further examine the Mn states in Mn/Al samples. As shown by the first-order derivatives of the XANES spectra in Figure S3, the Mn K edge spectrum of Mn/Al was not similar to those of either MnO, Mn_3O_4, Mn_2O_3, or MnO_2; therefore, the Mn species in Mn/Al might be a mixture of these species. The

Table 1. NO_2 Removal Capacity and NO Release with Various GHSV Values and Initial NO_2 Concentrations

	GHSV (h^{-1})							
	50 000		100 000		300 000			
samples	NO_2[a] mg/g	NO[b] mol %	NO_2[a] mg/g	NO[b] mol %	NO_2[a] mg/g	NO[b] mol %	NO_2[c] mg/g	NO[d] mol %
10 wt % Mn/Al[e]	175.8 ± 6.4	21.1 ± 1.3	196.7± 5.9	21.0 ± 1.6	247.6 ± 7.1	15.8 ± 2.0	5.0 ± 0.2	0
AC	91.1 ± 3.8	22.3 ± 1.5	84.4 ± 4.9	21.5 ± 2.7	42.6 ± 5.8	19.2 ± 3.1	0.9 ± 0.1	29.6 ± 2.4

[a]NO_2 removal capacity (mg_{NO_2}/g_{sample}) measured with an initial NO_2 concentration of 500 ppm. [b]NO release (mol %) measured with an initial NO_2 concentration of 500 ppm. [c]NO_2 removal capacity (mg_{NO_2}/g_{sample}) measured with an initial NO_2 concentration of 200 ppb. [d]NO release (mol %) measured with an initial NO_2 concentration of 200 ppb. [e]"±" presents standard deviation.

DOI: 10.1021/acs.est.9b00941
Environ. Sci. Technol. 2019, 53, 10855−10862

percentages of MnO, Mn_3O_4, Mn_2O_3, and MnO_2 species in Mn/Al were then calculated by linear fitting of the XANES spectra. The fitting data in Table 2 reveal that the Mn_3O_4, Mn_2O_3, and MnO_2 species coexisted in Mn/Al samples. With the increase in Mn loading amount, the Mn_3O_4 content increased and the Mn_2O_3 and MnO_2 contents decreased. When the Mn amount was increased to 10 wt %, the Mn_3O_4 content was approximately 70.2% in 10 wt % Mn/Al. Weakly crystalline Mn_3O_4 peaks in the XRD pattern of 8, 10, and 12 wt % Mn/Al suggested that Mn_3O_4 was well dispersed on the Al_2O_3 in a microcrystalline state, although the Mn_3O_4 content was high.

Table 2. Molar Ratio of Various Mn Oxides from the XANES Results of Mn K Edge of Mn/Al Samples

	molar ratio (%)		
Mn/Al	Mn_3O_4	Mn_2O_3	MnO_2
4 wt %	34.2	25.0	40.8
6 wt %	34.9	40.6	24.5
8 wt %	56.4	17.9	25.7
10 wt %	70.2	6.8	23.0
12 wt %	75.4	3.5	21.1
20 wt %	82.3	1.3	16.4

Brunauer–Emmett–Teller (BET) measurements were next conducted to examine the surface area and pore properties of the samples (Table S1). The surface areas of 4, 6, 8, 10, and 12 wt % Mn/Al samples show little difference. When the amount of Mn was increased to 20 wt %, the surface area decreased sharply, mainly due to pore blocking by MnO_x species. These results suggest that the surface area was not the crucial factor influencing the NO_2 removal efficiencies of Mn/Al materials.

Generally, it is difficult to distinguish Mn oxides and Al_2O_3 through microscopic imaging; thus, elemental mapping is necessary to identify Mn and its dispersion. Figure 3 shows the FETEM images and corresponding elemental mapping images of 4, 10, and 20 wt % Mn/Al samples. For 4 wt % Mn/Al, the distributions of Mn, Al, and O elements were nearly identical, indicating the high dispersion of Mn on the surface of Al_2O_3 (Figure 3a). In the case of 10 wt % Mn/Al, although a few larger Mn particles appeared (Figure 3b), Mn was still nanodispersed on the surface of Al_2O_3. When the loading amount of Mn was increased to 20 wt %, the distribution of Mn was obviously different from that of O and Al and the Mn oxides were no longer homogenously dispersed but aggregated into large particles. Based on these FETEM mapping and XRD results, it could be seen that high loading of Mn oxides induced better crystallinity but decreased the dispersion of active sites. When the loading amount of Mn oxides was low (such as 4 wt %), the removal efficiency was very low since there were insufficient active sites for NO_2 elimination. With increasing the loading amount from 4 to 10 wt %, more active sites were available on Al_2O_3, therefore improving the capacities of the Mn/Al materials. However, when the loading amount increased to 12 wt %, the Mn oxides began to show clear signs of aggregation (Figure S4). When the loading amount of Mn oxides was too high, such as 20 wt %, the Mn oxides aggregated into bigger clusters, resulting in the loss of active sites and thus decreasing the performance. Therefore, the 10 wt % Mn/Al sample exhibited the highest removal efficiency for NO_2 among the series of Mn/Al materials.

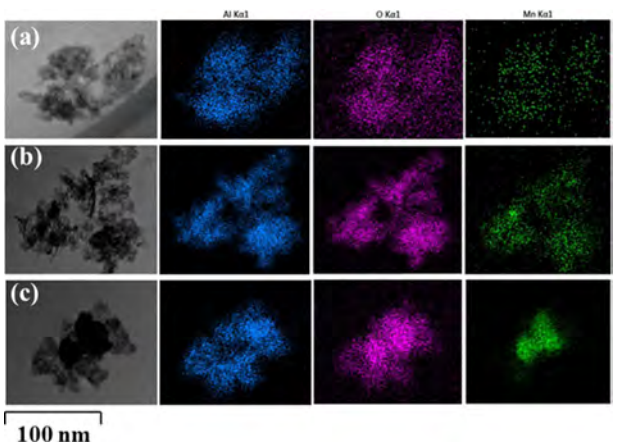

Figure 3. FETEM images and elemental mapping images of (a) 4, (b) 10, and (c) 20 wt % Mn/Al samples.

3.3. Effect of O_2 and H_2O on the NO_2 Removal Efficiency. NO_2 removal efficiencies were also examined for the Mn/Al samples in the absence of oxygen and in the presence of H_2O. As shown in Figure 4, the removal capacity of 10 wt % Mn/Al for NO_2 in N_2 was higher than that in air, implying that the presence of O_2 could affect the pathway of NO_2 adsorption related to the competition between adsorption and oxidation processes. The introduction of water vapor (relative humidity of 80%) also shortened the breakthrough time and dramatically decreased the NO_2 removal efficiency. A similar suppression effect induced by O_2 and water vapor also appeared for the AC and other Mn/Al samples (Figures 4, S5, and S6). It is important to note that the suppression effect of water vapor on NO_2 removal was reversible (Figure S7). When water vapor was removed from the reaction atmosphere, the removal efficiencies recovered to the same level as in the absence of water vapor. Such temporary suppression might be due to the competition between NO_2 and H_2O molecules on active sites.

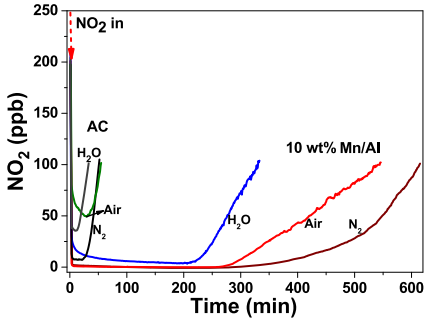

Figure 4. Comparison of NO_2 breakthrough curves in N_2, air, and air (RH 80%) at 25 °C. Reaction conditions: NO_2, 200 ppb; Mn/Al, 0.05 g; AC, 0.025 g; total flow rate, 1 L/min; GHSV, 300 000 h^{-1}.

3.4. Reaction Pathway in the Process of NO_2 Removal. The species formed on the surface of Mn/Al during the NO_2 abatement process were measured by time-resolved in situ DRIFTS (Figure S8), during which three main NO_2-related peaks appeared. The peaks at 1224 and 1482 cm^{-1} were assigned to the stretching vibration of nitrite and monodentate nitrate, respectively.[33−35] The weak peak at 1683 cm^{-1} is ascribed to the characteristic band of solvated nitric

DOI: 10.1021/acs.est.9b00941
Environ. Sci. Technol. 2019, 53, 10855−10862

acid.[34] The band at 1650 cm^{-1} is related to the adsorption of water due to the residual water vapor in the reaction atmosphere.[33] The above results indicate that adsorption, reduction, and oxidation processes simultaneously occurred during NO_2 removal on Mn/Al, mainly producing nitrite and nitrate species. Similar experiments were also performed on γ-Al_2O_3 and Mn_3O_4/Al_2O_3 prepared with commercial Mn_3O_4, with results shown in Figure S8a. Only the characteristic peak of absorbed water was observed on γ-Al_2O_3, and small amounts of nitrite and nitrate were formed on commercial Mn_3O_4/Al_2O_3, which was consistent with their low efficiencies for NO_2 elimination.

With the formation of surface nitrate and nitrite, two negative bands assignable to OH were observed at approximately 3744 and 3753 cm^{-1}.[36] These OH species should be related to the Mn site since the OH species on Al_2O_3 appeared at approximately 3750 cm^{-1} (Figure S8). The integrated areas of peaks due to nitrate, nitrite, and OH species were plotted as a function of reaction time (Figure 5a).[35] The

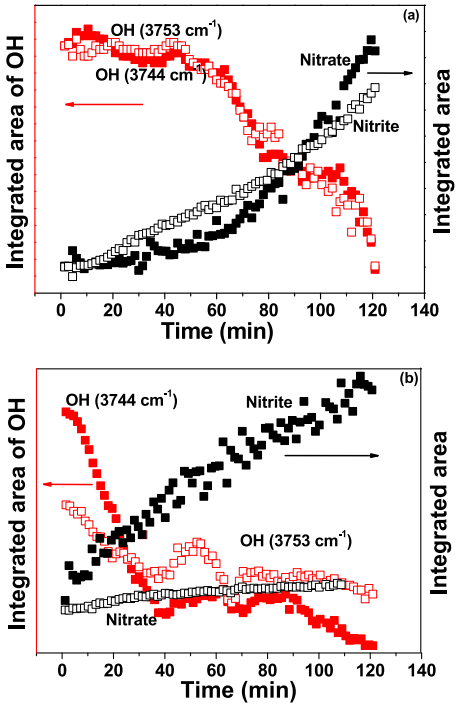

Figure 5. Comparison of the integrated areas of OH (3744 and 3753 cm^{-1}) with nitrite (1224 cm^{-1}) and nitrate (1482 or 1487 cm^{-1}) (a) in simulated air and (b) in N_2. Feed composition: NO_2, 200 ppb; total flow, 0.5 L/min.

increase in nitrate was always companied by a decrease in OH, which confirmed the important role of OH groups in NO_2 oxidation.[37,38] In contrast, the increased tendency of nitrite was not consistent with the decrease in OH, implying that OH groups were not responsible for the reduction of NO_2 to form nitrite because of the oxidizing properties of the OH groups. In the case of N_2 atmosphere, nitrites (1224 cm^{-1}), nitrates (1487 cm^{-1}), and soluble nitric acid (1680 cm^{-1}) appeared. The peak intensity of nitrite was notably higher than that of nitrate (Figure S8b), which is quite different from the result obtained in the case of air. Moreover, the increased tendencies of nitrite were not in good accordance with the decrease tendency of OH groups (Figure 5b), suggesting that OH groups did not play a key role in nitrite formation in the N_2 atmosphere.

Ion chromatography was used to measure the amounts of nitrate ions and nitrite ions on the Mn/Al samples (Table S2). In the case of the air atmosphere, the amount of nitrate was far higher than that of nitrite, further confirming the in situ DRIFTS results (Figure S8). Combined with the result in Figure 1, more than 70% of NO_2 was converted into nitrate and nitrite during NO_2 elimination. In the N_2 atmosphere, nitrite was the main product, and the amount of nitrate decreased compared to that in air. These findings indicated that the presence of O_2 was favorable for nitrate formation but detrimental to the formation of nitrite. When water vapor was introduced, the quantities of nitrate and nitrite decreased significantly due to the strong competitive adsorption between NO_2 and H_2O.

The XRD patterns of spent samples were also examined, exhibiting distinct differences between the ones reacted in air and N_2. For the samples used in the N_2 atmosphere, a new diffraction peak assigned to MnO_2 [PDF#42-1316] appeared at 21.6° (Figure S9), while no significant difference in the XRD pattern was observed in the spent Mn/Al in air (not shown), indicating that the Mn species played an important role in nitrite formation in the N_2. An XPS experiment was next performed to determine the Mn valence and active oxygen information. As shown in Figure S10, the Mn $2p_{3/2}$ spectra could be deconvoluted into two components of Mn^{3+} at 641.3 eV and Mn^{4+} at 643.4 eV.[39] Meanwhile, the O 1s spectra could be resolved into lattice oxygen at 529−530 eV and surface oxygen, including surface OH groups or oxide defects at 531−533 eV.[39,40] The fitting results in Table S3 exhibited that 10 wt % Mn/Al had the highest ratio of $Mn^{3+}/(Mn^{3+} + Mn^{4+})$, suggesting that Mn^{3+} ions were helpful for increasing the NO_2 adsorption and removal ability. After Mn/Al was tested in N_2 or in air, the amounts of both Mn^{3+} and lattice oxygen decreased, particularly in the former case. Therefore, it could be deduced that nitrite formation was mainly due to the reduction of NO_2 by low-valence Mn^{3+}, while nitrate mainly resulted from the reaction of NO_2 with OH groups or lattice oxygen.

Combining the in situ DRIFTS, XRD, and XPS results, the reaction pathway of NO_2 removal over Mn/Al was proposed (Figure 6). In the N_2 atmosphere, NO_2 adsorbed on the active

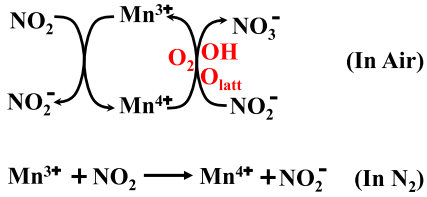

Figure 6. Diagram of the reaction pathway.

site of Mn^{3+} and reacted with Mn^{3+}, leading to the formation of nitrite and Mn^{4+}, which was the main reaction based on the amounts of nitrite and nitrate. In the air, the OH group played an important role in nitrate formation (as revealed by DRIFTS). It has been reported that surface OH groups are formed via water dissociation on oxygen vacancies[41−43] or on metal surfaces through water−oxygen interactions.[44−46] The OH species could promote O_2 adsorption and activation,[47,48] inducing the oxidation of NO_2 into nitrate. Furthermore, O_2 addition could supply lattice oxygen consumed in reactions,[49]

DOI: 10.1021/acs.est.9b00941
Environ. Sci. Technol. 2019, 53, 10855−10862

promoting the formation of nitrate with no change in the Mn valence. In other words, NO_2 removal with Mn/Al was mainly due to catalytic processes in air, while it mainly involved oxidation−reduction reaction processes in N_2. This is different from reported physisorption and chemisorption processes.[50] Whether in the air or N_2 atmosphere, Mn oxides were the active sites, playing the key role in NO_2 elimination. Al_2O_3 was the support for the Mn/Al materials, on which only physical adsorption occurred. Water molecules may occupy surface active sites and react partly with NO_2 on the surface of Mn/Al, resulting in the formation of soluble nitrate.

3.5. Regeneration of Mn/Al Material. Simple water washing was employed for the regeneration of the used Mn/Al. The used 10 wt % Mn/Al was first washed with deionized water followed by drying at 100 °C for 12 h in air. The as-prepared sample was then tested in air at room temperature, and the NO_2 breakthrough curves are shown in Figure 7. In

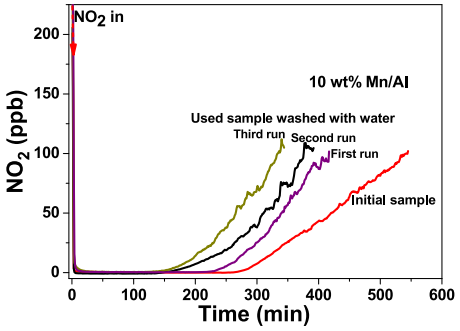

Figure 7. NO_2 breakthrough curves of the 10 wt % Mn/Al sample regenerated by water washing. Test conditions: NO_2, 200 ppb; Mn/Al, 0.05 g; total flow rate, 1 L/min (20 vol % O_2, N_2 balance); GHSV, 300 000 h^{-1}.

the first run, the removal ability of used Mn/Al recovered to 86% (4.3 mg/$g_{Mn/Al}$) of its initial level (5 mg/$g_{Mn/Al}$). Such incomplete recovery might be due to the conversion of Mn^{3+} into Mn^{4+} and a decrease in the O_{latt} contents (Table S3), which could not be recovered by washing. In the case of the second and third runs, the removal ability slowly decreased, showing the good reusability of Mn/Al via facile procedures. These findings show that the Mn/Al materials possessed excellent NO_2 abatement efficiency and suppressed the formation of NO and N_2O at room temperature. This low-cost and nanodispersed Mn_3O_4/γ-Al_2O_3 material with facile preparation and regeneration is a promising candidate material for atmospheric NO_2 abatement. For practical applications, however, the removal capacity and regeneration ability of the Mn/Al material should be tested and evaluated under practical conditions.

For combustion exhausts, NO is the main component of NO_x (~90% of total NO_x) at ppm levels, while NO_2 is usually dominant in the atmosphere at the ppb level (around 100 ppb). Therefore, these Mn/Al samples are more suitable for the elimination of ambient NO_2. In this study, we tested the materials with initial NO_2 levels of 200 ppb and 500 ppm, respectively. The NO_2 concentration of 200 ppb is close to that in the atmosphere; therefore, the testing results could demonstrate the capacity of Mn/Al for ambient NO_2 elimination. The testing with 500 ppm NO_2, on the one hand, aims to study the effects of initial NO_2 concentration on removal efficiency and, on the other hand, to compare the efficiency of Mn/Al with other reported materials since the measurements in previous studies have generally been performed under high NO_2 concentrations. To remove ambient NO_2 at ppb levels in indoor air or outdoor air, Mn/Al materials could be employed in air cleaners or painted onto indoor or outdoor buildings such as on walls, roads, panels, plasters, and other surfaces to improve the air quality, like photocatalysts.[51] An air cleaner usually contains a pump for air circulation and to increase the contact between contaminants and adsorption materials. In outdoor conditions, wind might be helpful for the increase of contact between contaminants and the materials.

Since the main contaminants in outdoor air are NO_2, O_3, SO_2, NH_3, and VOC species, the testing was also carried out in air with 200 ppb NO_2, 200 ppb O_3, 30 ppb SO_2, 20 ppb NH_3, and 20 ppb benzene as a typical VOC. In the coexistence of other gaseous pollutants, the results show that the breakthrough time was greatly extended, indicative of an improved ability of Mn/Al (Figure S11). It has been reported that coexisting SO_2 can increase the uptake coefficient of NO_2 on MgO.[52] NH_3 can promote the conversion of NO_2 to nitrate and nitrite species on the surface of α-Fe_2O_3.[53] Moreover, it has also been shown that VOCs could influence the heterogeneous reactions of NO_2,[54] and O_3 has strong oxidizing properties towards SO_2 and NO.[55] These previous studies could be helpful for us to understand the reasons for the improved efficiency of Mn/Al, but the detailed promotion mechanisms of different atmospheric contaminants need to be further investigated in future work.

■ ASSOCIATED CONTENT

Supporting Information

The Supporting Information is available free of charge on the ACS Publications website at DOI: 10.1021/acs.est.9b00941.

Sample preparation and characterization and NO_2 removal test, NO_2 breakthrough curves with difference GHSV and with coexistence of other gaseous pollutants, XANES patterns, XRD patterns, FETEM mapping images, XPS spectra and relevant analysis results, and BET and ion chromatography results (PDF)

■ AUTHOR INFORMATION

Corresponding Author

*E-mail: cbzhang@rcees.ac.cn. Tel: +86-10-62849801.

ORCID

Guangyan Xu: 0000-0002-4275-7517
Jinzhu Ma: 0000-0003-1878-0669
Yunbo Yu: 0000-0003-2935-0955
Qingxin Ma: 0000-0002-9668-7008
Kuo Liu: 0000-0001-7480-4480
Changbin Zhang: 0000-0003-2124-0620

Notes

The authors declare no competing financial interest.

■ ACKNOWLEDGMENTS

We sincerely thank Prof. Sijin Liu and Dr Yu Qi from the Research Center for Eco-Environmental Sciences, Chinese Academy of Sciences, for help preparing the manuscript. This work was financially supported by the National Key R&D Program of China (Nos. 2017YFC0211802, 2016YFC0207104, and 2017YFC0211101), the National

DOI: 10.1021/acs.est.9b00941
Environ. Sci. Technol. 2019, 53, 10855−10862

Natural Science Foundation of China (Nos. 51678560, 21673277), and the Youth Innovation Promotion Association, CAS (No. 2017064).

REFERENCES

(1) Zhao, B.; Wang, S. X.; Liu, H.; Xu, J. Y.; Fu, K.; Klimont, Z.; Hao, J. M.; He, K. B.; Cofala, J.; Amann, M. NO_x emissions in China: historical trends and future perspectives. *Atmos. Chem. Phys.* **2013**, *13*, 9869−9897.

(2) He, H.; Wang, Y. S.; Ma, Q. X.; Ma, J. Z.; Chu, B. W.; Ji, D. S.; Tang, G. Q.; Liu, C.; Zhang, H. X.; Hao, J. M. Mineral dust and NO_x promote the conversion of SO_2 to sulfate in heavy pollution days. *Sci. Rep.* **2015**, *4*, No. 4172.

(3) Sun, Y.; Jiang, Q.; Wang, Z. F.; Fu, P. Q.; Li, J.; Yang, T.; Yin, Y. Investigation of the sources and evolution processes of severe haze pollution in Beijing in January 2013. *J. Geophys. Res. Atmos.* **2014**, *119*, 4380−4398.

(4) Guo, S.; Hua, M.; Zamora, M. L.; Peng, J. F.; Shang, D. J.; Zheng, J.; Dua, Z. F.; Wu, Z. J.; Shao, M.; Zeng, L. M.; Molina, M. J.; Zhang, R. Y. Elucidating severe urban haze formation in China. *Proc. Natl. Acad. Sci. U.S.A.* **2014**, *111*, 17373−17378.

(5) Wang, Y. X.; Zhang, Q. Q.; Jiang, J. K.; Zhou, W.; Wang, B. Y.; He, K. B.; Duan, F. K.; Zhang, Q.; Philip, S.; Xi, Y. Y. Enhanced sulfate formation during China's severe winter haze episode in January 2013 missing from current models. *J. Geophys. Res. Atmos.* **2014**, *119*, 10425−10440.

(6) Ghafari, M.; Atkinson, J. D. Catalytic NO oxidation in the presence of moisture using porous polymers and activated carbon. *Environ. Sci. Technol.* **2016**, *50*, 5189−5196.

(7) Skalska, K.; Miller, J. S.; Ledakowicz, S. Trends in NOx abatement: A review. *Sci. Total Environ.* **2010**, *408*, 3976−3989.

(8) Ma, J. Z.; Wang, C. X.; He, H. Enhanced photocatalytic oxidation of NO over g-C_3N_4-TiO_2 under UV and visible light. *Appl. Catal., B* **2016**, *184*, 28−34.

(9) Wang, L.; He, H.; Zhang, C. B.; Wang, Y. F.; Zhang, B. Effects of precursors for manganese-loaded γ-Al_2O_3 catalysts on plasma-catalytic removal of o-xylene. *Chem. Eng. J.* **2016**, *288*, 406−413.

(10) Gao, X.; Liu, S.; Zhang, Y.; Luo, Z.; Ni, M.; Cen, K. Adsorption and reduction of NO_2 over activated carbon at low temperature. *Fuel Process. Technol.* **2011**, *92*, 139−46.

(11) Bashkova, S.; Bandosz, T. J. The effect of urea modification and heat treatment on the process of NO_2 removal by wood-based activated carbon. *J. Colloid Interface Sci.* **2009**, *333*, 97−103.

(12) Papailias, I.; Todorova, N.; Giannakopoulou, T.; Yu, J.; Dimotikali, D.; Trapalis, C. Photocatalytic activity of modified g-C_3N_4/TiO_2 nanocomposites for NO_x removal. *Catal. Today* **2017**, *280*, 37−44.

(13) Liu, F.; Yu, Y.; He, H. Environmentally-benign catalysts for the selective catalytic reduction of NOx from diesel engines: Structure-activity relationship and reaction mechanism aspects. *Chem. Commun.* **2014**, *50*, 8445−8463.

(14) Shirahama, N.; Moon, S. H.; Choi, K.-H.; Enjoji, T.; Kawano, S.; Korai, Y.; Tanoura, M.; Mochida, I. Mechanistic study on adsorption and reduction of NO_2 over activated carbon fibers. *Carbon* **2002**, *40*, 2605−2611.

(15) Belhachemi, M.; Jeguirim, M.; Limousy, L.; Addoun, F. Comparision of NO_2 removal using date pits activated carbon and modified commercialized activated carbon via different preparation methods: Effects of porosity and surface chemistry. *Chem. Eng. J.* **2014**, *253*, 121−129.

(16) Kante, K.; Deliyanni, E.; Bandosz, T. J. Interactions of NO_2 with activated carbons modified with cerium, lanthanum and sodium chlorides. *J. Hazard. Mater.* **2009**, *165*, 704−713.

(17) Levasseur, B.; Gonzalez-Lopez, E.; Rossin, J. A.; Bandosz, T. J. Effect of reduction treatment on copper modified activated carbons on NO_x adsorption at room temperature. *Langmuir* **2011**, *27*, 5354−5365.

(18) Peterson, G. W.; Mahle, J. J.; DeCoste, J. B.; Gordon, W. O.; Rossin, J. A. Extraordinary NO_2 removal by the metal-organic framework UiO-66-NH_2. *Angew. Chem., Int. Ed.* **2016**, *55*, 6235−6238.

(19) Angelo, J.; Andrade, L.; Madeira, L. M.; Mendes, A. An overview of photocatalysis phenomena applied to NOx abatement. *J. Environ. Manage.* **2013**, *129*, 522−539.

(20) Gandolfo, A.; Pouyer, L.; Wortham, H.; Gligorovski, S. The influence of wall temperature on NO_2 removal and HONO levels released by indoor photocatalytic paints. *Appl. Catal., B* **2017**, *209*, 429−436.

(21) Cassar, L. Photocatalysis of cementitious materials: Clean building and clean air. *MRS Bull.* **2004**, *29*, 328−331.

(22) Ballari, M. M.; Hunger, M.; Husken, G.; Brouwers, H. J. H. NOx photocatalytic degradation employing concrete pavement containing titanium dioxide. *Appl. Catal., B* **2010**, *95*, 245−254.

(23) Asadi, S.; Hassan, M.; Nadiri, A.; Dylla, H. Artificial intelligence modeling to evaluate field performance of photocatalytic asphalt pavement for ambient air purification. *Environ. Sci. Pollut. Res.* **2014**, *21*, 8847−8857.

(24) Brovelli, C.; Crispino, M. Photocatalytic suspension for road pavements: Investigation on wearing and contaminant effects. *J. Mater. Civ. Eng.* **2013**, *25*, 548−554.

(25) Carneiro, J. O.; Azevedo, S.; Teixeira, V.; Fernandes, F.; Freitas, E.; Silva, H.; Oliveira, J. Development of photocatalytic asphalt mixtures by the deposition and volumetric incorporation of TiO_2 nanoparticles. *Constr. Build. Mater.* **2013**, *38*, 594−601.

(26) Tang, X. F.; Li, J. H.; Sun, L.; Hao, J. M. Origination of N_2O from NO reduction by NH_3 over β-MnO_2 and α-Mn_2O_3. *Appl. Catal., B* **2010**, *99*, 156−162.

(27) Chang, H. Z.; Chen, X. Y.; Li, J. H.; Ma, L.; Wang, C. Z.; Liu, C. X.; Schwank, J. W.; Hao, J. M. Improvement of activity and SO_2 tolerance of Sn-modified MnO_x−CeO_2 catalysts for NH_3-SCR at low temperatures. *Environ. Sci. Technol.* **2013**, *47*, 5294−5301.

(28) Zhang, T.; Wang, D.; Gao, Z.; Zhao, K.; Gu, Y.; Zhang, Y.; He, D. Performance optimization of a MnO_2/carbon nanotube substrate for efficient catalytic oxidation of low-concentration NO at room temperature. *RSC. Adv.* **2016**, *6*, 70261−70270.

(29) Fan, X.; Zhu, T. L.; Wang, M. Y.; Li, X. M. Removal of low-concentration BTX in air using a combined plasma catalysis system. *Chemosphere* **2009**, *75*, 1301−1306.

(30) Ogata, A.; Miyamae, K.; Mizuno, K.; Kushiyama, S.; Tezuka, M. Decomposition of benzene in air in a plasma reactor: effect of reactor type and operating conditions. *Plasma Chem. Plasma Phys.* **2002**, *22*, 537−552.

(31) Shelef, M. Selective catalytic reduction of NOx with N-free reductants. *Chem. Rev.* **1995**, *95*, 209−225.

(32) Van Durme, J.; Dewulf, J.; Sysmans, W.; Leys, C.; Langenhove, H. V. Efficient toluene abatement in indoor air by a plasma catalytic hybrid system. *Appl. Catal., B* **2007**, *74*, 161−169.

(33) Ma, Q. X.; Liu, Y. C.; He, H. Synergistic effect between NO_2 and SO_2 in their adsorption and reaction on γ-Alumina. *J. Phys. Chem. A* **2008**, *112*, 6630−6635.

(34) Pozdnyakov, D.; Filimonov, V. Infrared spectroscopic study of the chemisorption of nitric oxide and nitrogen dioxide on metal oxides. *Kinet. Katal.* **1973**, *14*, 760.

(35) Goodman, A. L.; Bernard, E. T.; Grassian, V. H. Spectroscopic study of nitric acid and water adsorption on oxide particles: Enhanced nitric acid uptake kinetics in the presence of adsorbed water. *J. Phys. Chem. A* **2001**, *105*, 6443−6457.

(36) Van Veen, J. A. R.; Jonkers, G.; Hesselink, W. H. Interaction of transition-metal acetylacetonates with γ−Al_2O_3 surfaces. *J. Chem. Soc., Faraday Trans. 1* **1989**, *85*, 389−413.

(37) Kantcheva, M. Identification, stability and reactivity of NO_x species adsorbed on titania-supported manganese catalysts. *J. Catal.* **2001**, *204*, 479−494.

(38) Toops, T. J.; Smith, D. B.; Partridge, W. P. Quantification of the *in situ* DRIFTS spectra of Pt/K/gamma-Al_2O_3 NOx adsorber catalysts. *Appl. Catal., B* **2005**, *58*, 245−254.

DOI: 10.1021/acs.est.9b00941
Environ. Sci. Technol. 2019, 53, 10855−10862

(39) Tang, X.; Li, Y.; Huang, X.; Xu, Y.; Zhu, H.; Wang, J.; Shen, W. MnOx-CeO_2 mixed oxide catalysts for complete oxidation of formaldehyde: Effect of preparation method and calcinations temperature. *Appl. Catal., B* **2006**, *62*, 265−273.
(40) Li, Y.; Zhang, C.; Ma, J.; Deng, H.; He, H. High temperature reduction dramatically promotes Pd/TiO_2 catalyst for ambient formaldehyde oxidation. *Appl. Catal., B* **2017**, *217*, 560−569.
(41) Tang, H. L.; Wei, J. K.; Liu, F.; Qiao, B. T.; Pan, X. L.; Li, L.; Liu, J. Y.; Wang, J. H.; Zhang, T. Strong metal-support interactions between gold nanoparticles and nonoxides. *J. Am. Chem. Soc.* **2016**, *138*, 56−59.
(42) Zhang, Z.; Bondarchuk, O.; Kay, B. D.; White, J. M.; Dohnalek, Z. Imaging Water Dissociation on TiO_2 (110): Evidence for In equivalent Geminate OH Groups. *J. Phys. Chem. B* **2006**, *110*, 21840−21845.
(43) Vecchietti, J.; Bonivardi, A.; Xu, W.; Stacchiola, D.; Delgado, J. J.; Calatayud, M.; Collins, S. E. Understanding the role of oxygen vacancies in the water gas shift reaction on ceria-supported platinum catalysts. *ACS Catal.* **2014**, *4*, 2088−2096.
(44) Ojifinni, R. A.; Froemming, N. S.; Gong, J.; Pan, M.; Kim, T. S.; White, J. M.; Henkelman, G.; Mullins, C. B. Water-enhanced low-temperature CO oxidation and isotope effects on atomic oxygen-covered Au(111). *J. Am. Chem. Soc.* **2008**, *130*, 6801−6812.
(45) Bongiorno, A.; Landman, U. Water-enhanced catalysis of CO oxidation on free and supported gold nanoclusters. *Phys. Rev. Lett.* **2005**, *95*, 1−4.
(46) Kim, T. S.; Gong, J.; Ojifinni, R. A.; White, J. M.; Mullins, C. B. Water activated by atomic oxygen on Au(111) to oxidize CO at low temperatures. *J. Am. Chem. Soc.* **2006**, *128*, 6282−6283.
(47) Huang, H. B.; Leung, D. Y. C. Complete oxidation of formaldehyde at room temperature using TiO_2 supported metallic Pd nanoparticles. *ACS Catal.* **2011**, *1*, 348−354.
(48) Liu, L. M.; McAllister, B.; Ye, H. Q.; Hu, P. Identifying an O_2 supply pathway in CO oxidation on Au/TiO_2(110): A density functional theory study on the intrinsic role of water. *J. Am. Chem. Soc.* **2006**, *128*, 4017−4022.
(49) Shang, Z.; Sun, M.; Chang, S.; Che, X.; Gao, X.; Wang, L.; Guo, Y.; Zhan, W.; Guo, Y.; Lu, G. Activity and stability of Co_3O_4-based catalysts for soot oxidation: The enhanced effect of Bi_2O_3 on activation and transfer of oxygen. *Appl. Catal., B* **2017**, *209*, 33−44.
(50) Ruiz-Soria, G.; Paz, A. P.; Sauer, M.; Mowbray, D. J.; Lacovig, P.; Dalmiglio, M.; Lizzit, S.; Yanagi, K.; Rubio, A.; Goldoni, A.; Ayala, P.; Pichler, T. Revealing the adsorption mechanisms of nitroxides on ultrapure, metallicity-sorted carbon nanotubes. *ACS Nano* **2014**, *8*, 1375−1383.
(51) Chen, M.; Chu, J. W. NOx photocatalytic degration on active concrete road surface-from experiment to real-scale application. *J. Cleaner Prod.* **2011**, *19*, 1266−1272.
(52) Ma, Q. X.; Wang, T.; Liu, C.; He, H.; Wang, Z.; Wang, W. H.; Liang, Y. T. SO_2 initiates the efficient conversion of NO_2 to HONO on MgO. *Environ. Sci. Technol.* **2017**, *51*, 3767−3775.
(53) Yang, W. W.; Ma, Q. X.; Liu, Y. C.; Ma, J. Z.; Chu, B. W.; Wang, L.; He, H. Role of NH_3 in the heterogeneous formation of secondary inorganic aerosols on mineral oxides. *J. Phys. Chem. A* **2018**, *122*, 6311−6320.
(54) Sun, Z. Y.; Kong, L. D.; Zhao, X.; Ding, X. X.; Fu, H. B.; Cheng, T. T.; Yang, X.; Chen, J. M. Effect of formaldehyde on the heterogeneous reaction of nitrogen dioxide on γ-alumina. *J. Phys. Chem. A* **2015**, *119*, 9317−9324.
(55) Liu, W. J.; He, X.; Pang, S. F.; Zhang, Y. H. Effect of relative humidity on O_3 and NO_2 oxidation of SO_2 on α-Al_2O_3 particles. *Atmos. Environ.* **2017**, *167*, 245−253.

DOI: 10.1021/acs.est.9b00941
Environ. Sci. Technol. 2019, 53, 10855−10862